Available online at www.sciencedirect.com
ScienceDirect
Journal of Sound and Vibration 313 (2008) 493–509
JOURNAL OF SOUND AND VIBRATION
www.elsevier.com/locate/jsvi

# Mid-frequency response of structures with integral compliant mechanisms: Verification and validation

E.M. Dede*, G.M. Hulbert

*Department of Mechanical Engineering, The University of Michigan, Ann Arbor, MI 48109-2125, USA*

Received 26 February 2007; received in revised form 5 December 2007; accepted 17 December 2007
Handling Editor: P. Davies
Available online 31 January 2008

**Abstract**

Sandwich structures with designed cellular solid or truss cores are well known to possess desirable mechanical properties, including large stiffness-to-weight ratios and vibration/acoustic isolation. Practical applications include the design of lightweight vehicle structures and multi-functional structural–acoustic linings. In this paper, a novel use of compliant mechanisms as the core topology is presented to attenuate mid-frequency structural response of sandwich structures. The effectiveness of integral compliant mechanisms for dynamic response attenuation is demonstrated through computational analysis and experimental investigation of both a designed integral compliant mechanism structure and a more conventional square core structure. It is verified that one-dimensional spectral finite element analyses are appropriate for the initial design of a prototype structure, but validation requires conventional finite element analyses to properly model the as-built geometric complexity.


## 1. Introduction

Structures that vibrate in the 1–10 kHz frequency range generate noise [1–3]. In contrast to lower-frequency vibrations in which the modes of vibration have relatively long wavelengths (relative to the size of the structure), these mid-frequency vibrations are characterized by more local modes of deformation, with wavelengths that are short relative to the structure of interest. Various solutions to structural-borne sound exist ranging from conventional approaches, such as viscoelastic coatings, to alternative designs that include periodic lattices and structures [4–6]. These particular periodic structures are a class of sandwich structures. Consequently, their high stiffness-to-weight ratio and mid-frequency isolation attributes both are attractive for the design of practical engineering structures.

The square core truss shown in Fig. 1 is frequently considered as an example periodic sandwich structure comprising multiple square core unit cell building blocks that are connected end to end [4,6]. Such structures have reduced mass, yet are capable of supporting large static loads. These global structural characteristics are

*Corresponding author. Tel.: +1 734 764 8254.
*E-mail address:* dedeem@umich.edu (E.M. Dede).

0022-460X/$ - see front matter © 2007 Elsevier Ltd. All rights reserved.
doi:10.1016/j.jsv.2007.12.021

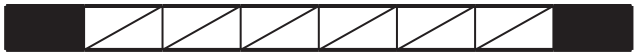

Fig. 1. Periodic square core sandwich structure (0.6 m × 0.055 m).

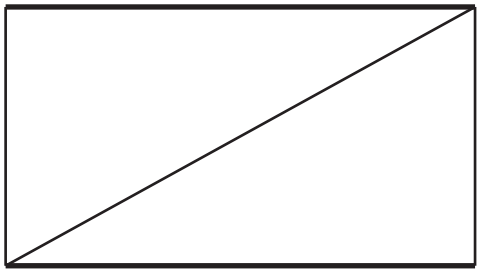

Fig. 2. Square core unit cell (0.1 m × 0.055 m).

a consequence of the topology of the local unit cell given in Fig. 2, which consists of a thin walled rectangle braced by a diagonal member.

The dynamic analysis of periodic structures is commonly carried out by exploiting their aforementioned local–global nature; the behavior of the local unit cell is used as a predictor of global structural dynamic response [4,6,7]. This multi-scale approach reduces computational time and is founded on earlier studies of wave propagation in periodic lattices, plates, and shells [8–10]. Recently, other novel multi-scale techniques for the analysis and design of similar structures have been developed to control dynamic response [11–13]. Moreover, experimental investigation of the dynamic properties of periodic structures is garnering greater interest [14].

To design more effective periodic lattice structures, a different direction has been taken in our research. The sound level emanating from a structure's surface is proportional to the transverse velocity (normal velocity) of the surface. Thus, for a sandwich structure, it is desirable to minimize the vibration amplitude on the output side relative to the motion of the input side of the structure. This output/input relationship is related to the concept of mechanical advantage, which is used typically to characterize the quasi-static performance of kinematic mechanisms. Assuming power conservation, for a given input speed, $v_{\text{in}}$, the output speed, $v_{\text{out}}$, can be reduced by seeking a mechanism topology with a large mechanical advantage (MA):

$$\text{MA} = \frac{v_{\text{in}}}{v_{\text{out}}}. \tag{1}$$

One good candidate mechanism is the rigid link rhombus straight-line mechanism, depicted in Fig. 3. In this figure one-half of the symmetric mechanism is shown, where the empty circles denote revolute joints. This linkage is inspired by Model S39 from the Reuleaux Collection of Kinematic Mechanisms at Cornell University [15]. To extend the use of mechanical advantage from the scalar output-to-scalar input definition, a 'unit cell' concept is employed in which the unit cell is the basic framework into which a mechanism topology can be placed in order to reduce locally the output response of the structure. Then, multiple unit cells can be assembled to construct a globally periodic structure that has enhanced vibro-acoustic characteristics.

Rather than attempt to embed rigid link mechanisms into a structure, a more practical method is to employ multiple compliant mechanisms that are integrated into the structure. This approach utilizes and extends the breadth of research that has already been performed for standalone compliant mechanisms, e.g. Refs. [16,17]. Accordingly, a compliant mechanism design is shown in Fig. 4 that corresponds to the rigid link mechanism of Fig. 3; the rhombus straight-line mechanism was chosen based upon its optimum topology for compliant mechanisms with a large mechanical advantage [18]. A conceptual model of a compliant mechanism structure, which is an assemblage of six unit cells, is given in Fig. 5.

The purpose of this paper is to demonstrate the applicability of integral compliant mechanisms for attenuating mid-frequency vibration of structures. To this end, the manuscript is organized as follows. Section 2 presents an overview of the compliant mechanism prototype design. Results from efficient one-dimensional finite element (frame element) spectral analyses are presented both for the compliant mechanism

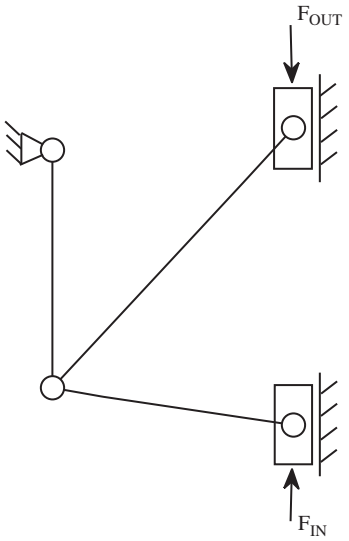


Fig. 3. Rigid link diagram of one half of rhombus mechanism.

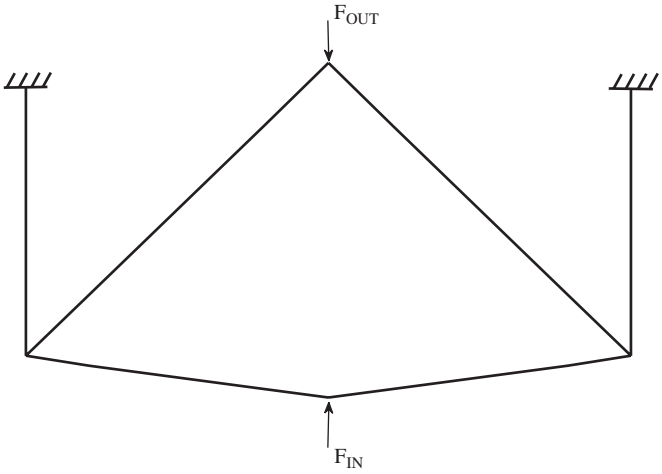


Fig. 4. Rhombus compliant mechanism design.

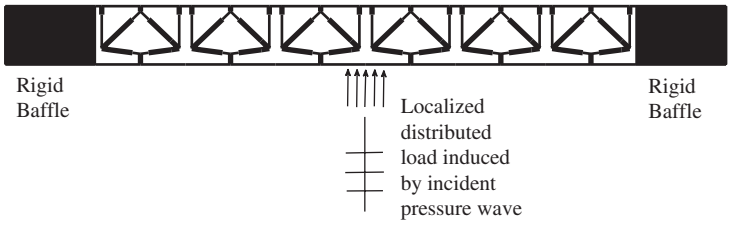


Fig. 5. Periodic compliant mechanism structure (0.6 m × 0.055 m).

prototype unit cell and for a structure comprising six compliant mechanism cells. Also presented are corresponding analytical results for a square core truss unit cell and six-cell structure, which serve as the reference designs. Section 3 describes the fabrication and experimental test setup for the compliant mechanism and square core truss structures. In Section 4, comparisons are made between the experimental results and

results from the spectral finite element analyses. Although the applicability is validated of using integral compliant mechanisms for vibration attenuation, significant differences occur between the experimental results and the spectral finite element analysis results. Better agreement with the experimental results is shown using results from conventional (two-dimensional) finite element analyses. A two-stage design and analysis process is recommended in Section 5, along with conclusions and suggested future research directions.

## 2. Prototype design and analysis

An overview of the compliant mechanism prototype design is presented in this section. Spectral finite element analyses were performed using one-dimensional (frame) spectral elements. Results are described from analyses of the reference square core unit cell and the reference square core truss structure. Results from spectral finite element analyses of the compliant mechanism unit cell and integral compliant mechanism structure are presented and compared with those from the reference unit cell and structure. More details can be found in Ref. [19].

### 2.1. Prototype design

As depicted in Fig. 5, an incident pressure wave loads the structure's input (bottom) surface, which, in this work, is a beam. Mid-frequency response for this beam is characterized by transverse wave propagation. For the design of mid-frequency attenuation mechanisms, the objective is to isolate the top surface (beam) from transverse wave propagation through the bottom beam by invoking the principle of mechanical advantage via passive mechanism actuation. Fig. 4 presents a compliant mechanism design to achieve this objective and Fig. 6 depicts the unit cell model for this design. For this model, the sliders in the rigid link diagram of Fig. 3 are enforced using symmetry about the vertical centerline of the unit cell. The 'ground' elements for the mechanism, elements 3 and 23, are attached to the unit cell top layer so that mid-frequency transverse waves can propagate unimpeded through the bottom layer. In the present context, 'ground' designates a point of reference measurement, rather than an immovable location. While the ground elements can (and do) move, the goal is to minimize the difference in the transverse (vertical) motions of points 13 and 5, relative to the difference in the transverse motions of points 11 and 5. In other words, local deformation (wavelengths of the order of the unit cell length) minimization is desired.

To predict the frequency at which attenuation begins, the frequency–wavelength relationship for transverse waves propagating through a beam is invoked, per [19]

$$\omega = \left(\frac{2\pi}{\lambda}\right)^2 \sqrt{\frac{EI}{\rho A}}, \tag{2}$$

where $\omega$ is the frequency; $\lambda$ is the wavelength; $\rho$, $E$, $A$ and $I$ are the bottom layer beam material density, Young's modulus, cross-sectional area and area moment of inertia, respectively. As frequency, $\omega$, increases and the wavelength of vibration, $\lambda$, approaches the length scale of the unit cell, the motion of the top layer of the structure is reduced through the actuation of the integral compliant mechanism. For a given bottom layer

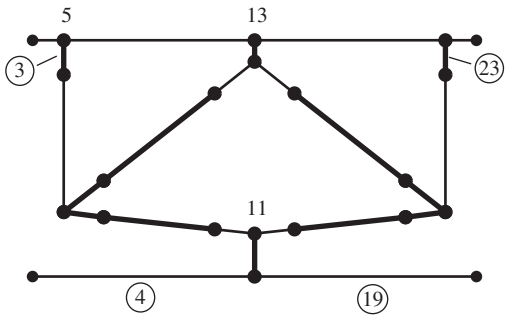


Fig. 6. Rhombus compliant mechanism unit cell model (0.1 m × 0.055 m). Numbers that are circled denote elements, numbers that are not circled denote nodes.

configuration and a desired starting (minimum) attenuation frequency, Eq. (2) can be used to determine the length of the compliant mechanism unit cell; i.e., unit cell length $= \lambda$.

### 2.2. Prototype analysis using one-dimensional spectral elements

Numerical analyses were performed using one-dimensional linear spectral finite elements based on the method outlined in Ref. [20]. A frequency step of 10 Hz was used for all analyses.

For the unit cell analysis, boundary conditions are applied to the nodes on the left and right edges of the unit cell that are representative of the boundary conditions imposed on the unit cell when assembled into the structure. This corresponds to constraining the rotational degrees-of-freedom of all nodes on the left and right edges of the unit cell while leaving the translational degrees of freedom unconstrained. For the assembled structure, the rigid baffles are modeled using fixed–fixed boundary conditions.

In accordance with the manufactured structures, the unit cell and structure are assumed to be made of 6061-T6 aluminum with $E = 6.83 \times 10^{10}\,\mathrm{N/m^2}$, and $\rho = 2713.6\,\mathrm{kg/m^3}$, per Ref. [21]. Hysteretic material damping is introduced to account for inherent energy loss, and following Refs. [4,6], a complex modulus, $E^* = E(1 + i\eta)$, is utilized with $\eta = 0.01$.

The square core unit cell model, Fig. 2, is assumed to have dimensions of 0.1 m (length) × 0.055 m (height) × 0.0127 m (out-of-plane depth). The top and bottom facesheet widths are shown as thicker lines and are 5 mm wide while thinner lines representing core members have a width of 2.5 mm. The overall dimensions of the six unit cell reference square core structure illustrated in Fig. 1 are 0.6 m × 0.055 m × 0.0127 m.

The sizing of individual members within the compliant mechanism unit cell is similar to that of the members in the conventional square core unit cell. In Fig. 6 thicker lines represent stiffer elements having a width of 5 mm while thinner lines represent elements 2.5 mm wide. Given the bottom layer physical parameters ($\rho$, $E$, $A$, and $I$), the overall compliant mechanism unit cell length is determined using the frequency–wavelength relationship, Eq. (2), along with a selected attenuation zone starting frequency of 2320 Hz. Accordingly, similar unit cell dimensions of 0.1 m × 0.055 m are used, leading to a compliant mechanism with a mechanical advantage of 7.0. Assuming a compliant mechanism structure composed of six unit cells, the same global structure dimensions are obtained (i.e. 0.6 m × 0.055 m × 0.0127 m).

A uniform pressure amplitude loading across the unit cell bottom layer is assumed. The spectral nodal loading equivalent to the incident pressure wave on a bottom layer element, $e$, of the unit cell and structure is given, per Ref. [19], as

$$\hat{\mathbf{f}}^e(\hat{\mathbf{w}}_b, \omega) = \int_0^{L^e} \hat{\mathbf{w}}_b(x, \omega) p_{\mathrm{in}}\, \mathrm{d}x, \tag{3}$$

where $\hat{\mathbf{w}}_b$ is the spectral weighting function for the beam element, $L$ is the length of the element, and $p_{\mathrm{in}}$ is the normally incident pressure wave amplitude. For the unit cell analysis, $p_{\mathrm{in}} = 1\,\mathrm{N/m^2}$.

For the structure, to approximate the loading from the loudspeaker in the experiments, a localized sound pressure level amplitude of 145.4 dB re 20E−6 Pa is assumed to act over a 0.025 m wide × 0.0127 m deep area centered about the middle of the bottom layer of the structure (refer to Fig. 5). This loading was converted to an equivalent nodal loading on the bottom layer for the affected nodes.

### 2.3. Spectral finite element analysis results

Sound in a fluid domain is linked to pressure level variation, which depends upon the normal velocity of a radiating object. Consequently, the root-mean-square (rms) normal velocity of a structure has been the figure of merit for evaluating structural dynamic response [4,6]. The rms transverse velocity response, suggested in Ref. [4], is computed in decibels as

$$v_{\mathrm{rms}} = 20 \log_{10} \left[ \frac{\omega}{v_{\mathrm{ref}}} \left[ \frac{1}{N} \sum_{j=1}^{N} |\hat{v}_j^t|^2 \right]^{1/2} \right], \tag{4}$$

where $\omega$ is the frequency of interest, $v_{\text{ref}}$ is a reference velocity, $\hat{v}_j^l$ is the transverse spectral displacement of the $j$th node of interest, and $N$ is the number of top layer nodes. Unless otherwise stated, $v_{\text{rms}}$ is computed using $v_{\text{ref}} = 10^{-8}$ m/s throughout the remainder of this work.

Clearly, this pointwise sampling approach to computing the top layer normal velocity is an approximation. As the number of top layer nodes sampled is increased, the error in the computed metric will decrease, leading to a better estimate of the noise generated in the fluid domain above a given structure. In the present work the distance between the sampled nodes on the top layer of a unit cell/structure is of the order of the wavelength of vibration. As such, the salient mid-frequency traits of the structural dynamic response are captured and thus, the pointwise approximation is reasonable.

The frequency response function output to input amplitude and phase of the compliant mechanism unit cell model are defined by the following relationships:

$$\text{Amplitude} = \left|\frac{\hat{v}_{13} - \hat{v}_5}{\hat{v}_{11} - \hat{v}_5}\right|; \quad \text{Phase} = \frac{180}{\pi}[\angle(\hat{v}_{13} - \hat{v}_5) - \angle(\hat{v}_{11} - \hat{v}_5)], \tag{5}$$

where the unit cell output is taken as the transverse spectral displacement, $\hat{v}$, of node 13 relative to node 5, while the input is taken as the transverse spectral displacement of node 11 relative to node 5. Node 5 is selected since it represents part of the 'ground' of the mechanism. Ideally, the rhombus mechanism is intended to operate as an 'inversor' where the input and output motions are 180°out-of-phase. Accordingly, the frequency response function relationships, Eq. (5), provide insight into the performance of the compliant mechanism unit cell distinguishing out-of-phase, non-resonant performance from in-phase, resonant performance [19].

The rms transverse velocity of the reference square core unit cell is provided over the frequency range of 0–10 kHz in Fig. 7. In Fig. 8 the rms transverse velocity of the six unit cell reference square core structure, computed using the response from all top layer nodes, i.e. $N = 5$ in Eq. (4), is shown. Comparison of these two figures reveals that the dynamic response of the unit cell is an accurate predictor of the dynamic response of the structure. Exceptions include the first global resonance of the structure visible at 590 Hz, Fig. 8, and increased modal density between the computed peaks in response at 1050, 2550, 3580, 5520, and 9500 Hz. The largest response levels above 1 kHz for the unit cell and structure occur between 3300 and 4000 Hz and are followed by a significant anti-resonance between 4500 and 5500 Hz. Note that at 4630 Hz the wavelength of vibration (for transverse waves traveling through the bottom layer of the reference unit cell) equals the length scale of the unit cell, per Eq. (2).

The computed rhombus compliant mechanism unit cell frequency response function and rms transverse velocity are given in Fig. 9 for the frequency range 0–10 kHz. Observe that each curve in Fig. 9 has a different

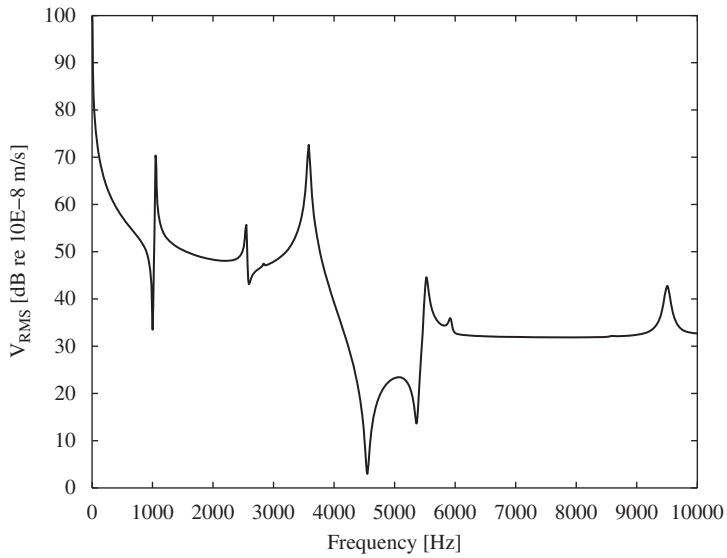


Fig. 7. Spectral finite element top layer root-mean-square velocity for reference square core unit cell.

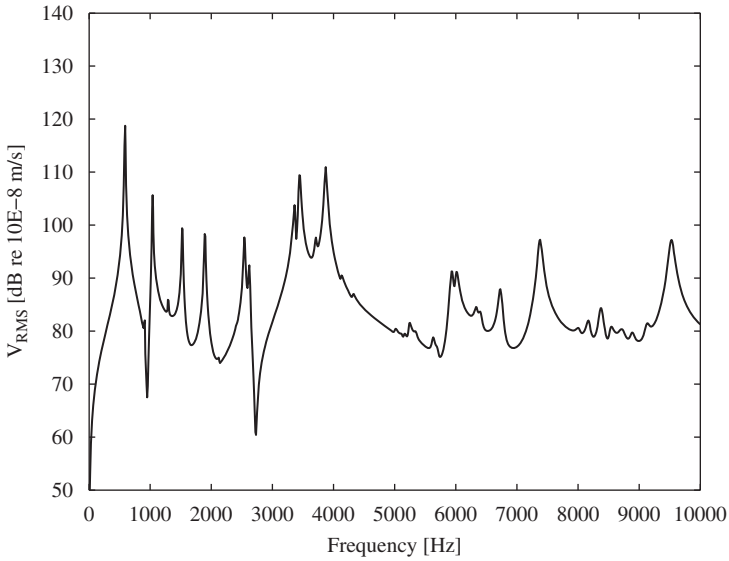


Fig. 8. Spectral finite element top layer root-mean-square velocity (computed using the response from all top layer nodes) for reference square core structure.

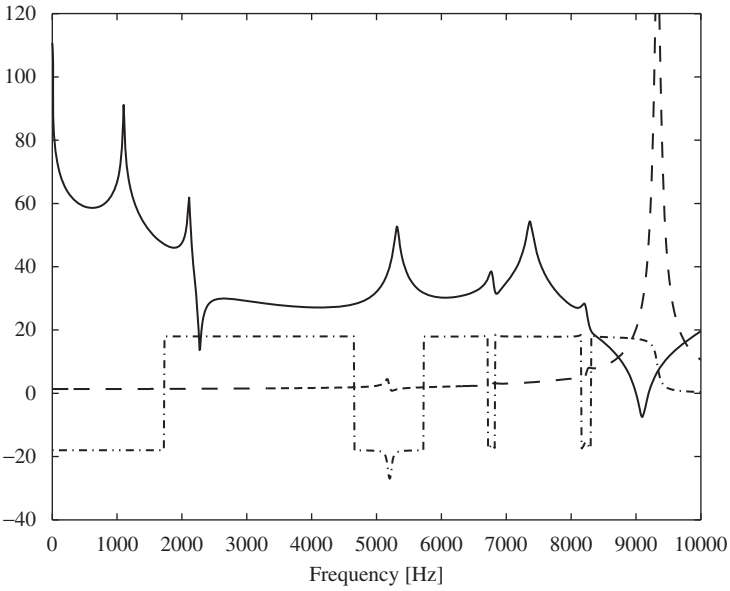


Fig. 9. Spectral finite element compliant mechanism unit cell frequency response function. (——) $v_{rms}$ [dB re $10^{-8}$ m/s], (– –) 10 × amplitude, (– · –) 0.1 × phase angle [deg].

set of units for the ordinate axis as provided in the figure caption. Additionally, the amplitude and phase curves in Fig. 9 are, respectively, scaled by factors of 10 and 1/10 for visual clarity. Below 2320 Hz, peaks in response are observed at 1100 and 2110 Hz. Above 2320 Hz, two major attenuation zones are present spanning the frequency ranges of 2320–5300 and 9240–9500 Hz. At the starting frequencies of these attenuation zones, the wavelength of vibration for transverse waves in the unit cell bottom layer equals the unit cell width and half-width, respectively, per Eq. (2). Observe that the breadth of the first attenuation zone for the compliant mechanism unit cell is significantly larger than the breadth of the anti-resonance for the reference square core unit cell at 4630 Hz in Fig. 7. Within each attenuation zone the mechanism demonstrates out-of-phase, non-resonant (small amplitude) behavior, as expected. Between the attenuation zones (i.e. 5300–9240 Hz) in-phase,

resonant behavior is exemplified by peaks in the rms transverse velocity response, increases in the frequency response function amplitude, and a frequency response function phase that transitions away from 180°. Similar increases in response are visible immediately after the second attenuation zone starting frequency of 9240 Hz. Just above this frequency, the rms normal velocity response increases slightly, however a more prevalent peak in the frequency response function amplitude is present in conjunction with a frequency response function phase angle that moves from out-of-phase (i.e. 180°) towards in-phase (i.e. 0°).

The rms transverse velocity of the compliant mechanism structure, computed using the response from all top layer nodes, i.e. $N = 23$ in Eq. (4), is given in Fig. 10. The first global resonance of the structure occurs at

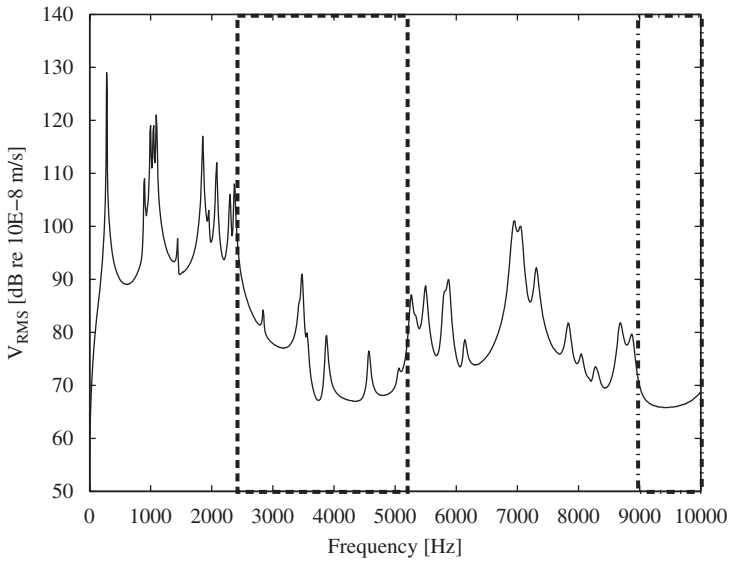


Fig. 10. Spectral finite element top layer root-mean-square velocity (computed using the response from all top layer nodes) for compliant mechanism structure. (– –) First attenuation zone, (– · –) second attenuation zone.

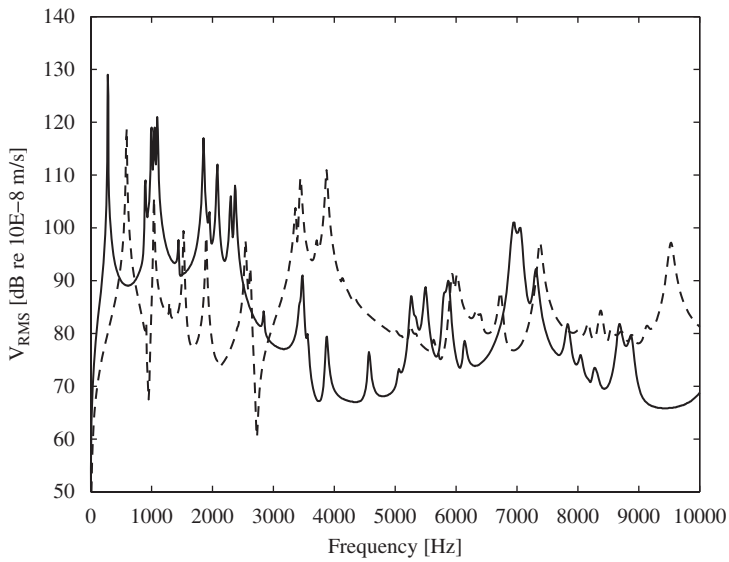


Fig. 11. Spectral finite element top layer root-mean-square velocity comparison (computed using the response from all top layer nodes). (– –) Reference square core structure, (——) compliant mechanism structure.

230 Hz. Unit cell resonances at 1100 and 2110 Hz are visible in the response of the structure along with increased modal density. The first attenuation zone exists between approximately 2500 and 5200 Hz with the occurrence of four smaller amplitude resonant peaks. Between 5 and 9 kHz structural dynamic response increases as expected based on the response of the unit cell, and above 9 kHz the second attenuation zone is visible. Low-amplitude resonances within the first attenuation zone emanate from global, structural modes that are not captured by the unit cell analysis. Nonetheless, given the overall breadth of the 10 kHz frequency range, the general structural dynamic characteristic of interest is verified at the global, structural level.

In Fig. 11 a direct comparison is made between the rms transverse velocity response of the reference square core structure and the compliant mechanism structure. In the first attenuation zone for the compliant mechanism structure, between 2500 and 5200 Hz, an average reduction in response of 11.6 dB is present. Within the second attenuation zone for the compliant mechanism structure, from 9 to 10 kHz, an average reduction of 15.8 dB is observed. In comparison with the reference square core sandwich structure, the compliant mechanism sandwich structure has significantly lower levels of dynamic response over these two broadbands of the mid-frequency range.

## 3. Prototype manufacturing and experimental test setup

A standard three-axis computer-numerically controlled mill was used to fabricate the prototype compliant mechanism and reference square core structures. The structures were manufactured by exporting three-dimensional solid model geometry to data files and importing those files into computer-aided manufacturing software to generate the machining tool paths for the milling operations. The pocket geometry was machined using a 1/8-in diameter end mill.

The experimental test setups for the reference square core structure and compliant mechanism structure are shown in Figs. 12 and 13, respectively. Fixed–fixed boundary conditions were enforced by mounting each end of each structure to a steel standoff, which was then rigidly attached to an optical bench. Each test setup was designed to minimize inadvertent excitation of torsional and out-of-plane bending modes.

Following Ref. [22], a non-contacting excitation and measurement method was utilized to minimize the effects of the experimental setup on the structure's inherent dynamic properties. Local forcing was achieved using a 0.025 m diameter tweeter, VIFA model DX25TG05-04, positioned 0.64 mm from the center of the structure's bottom layer. The diameter of the loudspeaker was selected to match the length over which the localized distributed load was applied in the computational analysis. Care was taken to assure the loudspeaker diaphragm did not touch the structure during testing. A first-order (i.e. six decibels per octave) high-pass filter with a crossover frequency of 500 Hz was connected in series with the loudspeaker to allow pure harmonic

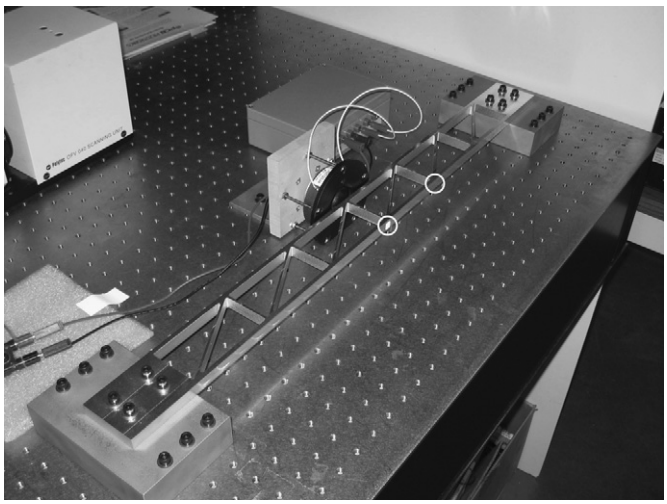

Fig. 12. Experimental test setup for reference square core structure. Circled regions denote measurement locations.

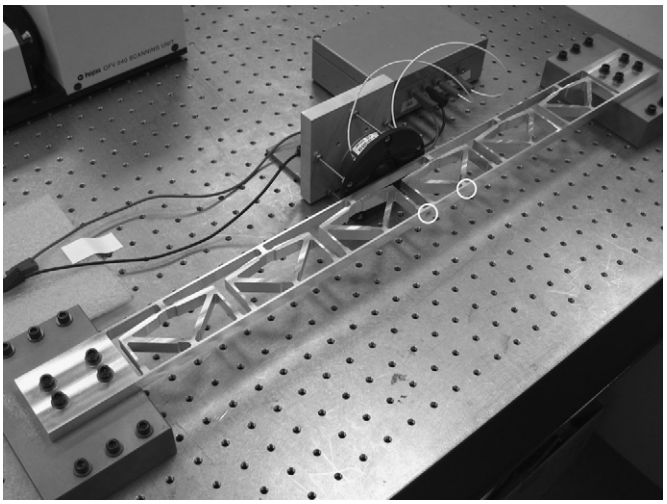

Fig. 13. Experimental test setup for compliant mechanism structure. Circled regions denote measurement locations.

stepped-sine excitation in the frequency range of 1–10 kHz at 10 Hz frequency intervals. A standard personal computer with *LabVIEW* software and an analog output channel were used as a signal generator. The sinusoidal signal then was sent to the loudspeaker via an amplifier, Adcom model GFA-535, and the high-pass filter. Response was measured using a non-contacting single point laser vibrometer, Polytec model OFV-2602 with OFV-353 optics. A total of 901 data points were taken per measurement location for each structure. The single point laser vibrometer output voltage was measured using an oscilloscope, Agilent model 54621A. The oscilloscope output voltage was then converted to a velocity magnitude using the appropriate laser vibrometer scale factor. Sufficient dwell time between frequency steps was taken to ensure that transient response did not affect test measurements, per Ref. [23].

Two measurement locations were monitored for each structure as highlighted in the circled regions of Figs. 12 and 13. The top layer center point and a point 0.1 m off of center was used for the reference square core structure. These measurement locations represent the point of maximum displacement and a point exactly one bay over, respectively. For the integral compliant mechanism structure the top layer center point and a point 0.05 m off of center was used. These two measurement locations were selected since they represent the point of maximum displacement and a compliant mechanism output node, respectively.

Prior to testing, the loudspeaker was calibrated in an anechoic chamber using 8 W of power at 1 m using a Larson-Davis 2520 microphone and 2200C preamplifier. Scaling the measured sound pressure level at 1 m to a distance of 0.64 mm allowed for the calculation of an input sound pressure level to the structure of approximately 145.4 dB re 20E−6 Pa. This allows for direct comparison of the experimentally measured response of each structure with the corresponding computational result. The sensitivity of the loudspeaker was such that a relatively flat response was obtained across the 1–10 kHz test frequency range. This precluded concerns of input pressure fluctuations, and hence, local forcing variation.

## 4. Verification and validation

In this section, all rms transverse velocity responses are computed with $N = 2$ in Eq. (4), in which the locations of the two nodes correspond to the locations of the experimental measurements as described in the previous section.

### 4.1. Comparison of experiment and spectral finite element analyses

In Fig. 14 the rms transverse velocity response of the square core structure, computed using the spectral finite element method, is compared with experimentally obtained results. Significant differences can be

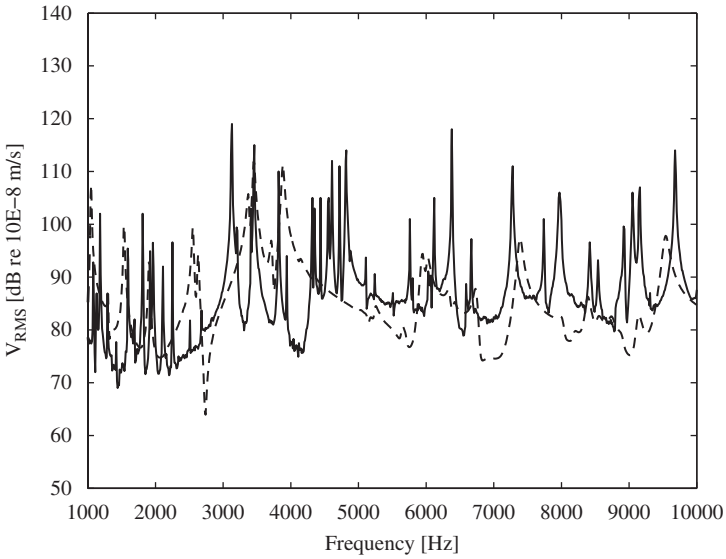


Fig. 14. Spectral finite element versus experimental root-mean-square transverse velocity (computed using the response from two top layer nodes) for square core structure. (– –) Spectral data, (——) experimental data.

observed between the computational and experimental results. The experimental data exhibits greater modal density, larger resonant amplitudes, and a shifting of response towards higher frequencies. Specifically, the experimental data for the square core structure show many more resonances below 3 kHz. The two peaks around 4 kHz that dominate the computational response are split into two broader bands of resonant peaks spanning 3–5 kHz in the experimental data. Above 5 kHz, response matches in an approximate sense, however the amplitude of resonance and the sharpness of each peak at 6380 and 9680 Hz in the experimental data suggests lower levels of structural damping. Better agreement in the amplitude and sharpness of the resonance peaks could be attained by decreasing the assumed value of the loss factor ($\eta = 0.01$ for the results presented). However, the dynamic response characteristics of most importance for this work are the starting frequencies and bandwidths of the attenuation zones, as the objective is to design structures with prescribed attenuation zones. Thus, note that the bandwidth of the attenuation zone in Fig. 14 for the manufactured square core structure spans 5000–5500 Hz (a slightly reduced range when compared with the spectral data).

Similar differences can be observed in Fig. 15 in which the experimental and computational results of the compliant mechanism structure are compared. The shift of measured response towards higher frequencies is more noticeable, which implies that the physical prototype is substantially stiffer than the computational model predicts. Despite these differences, upon closer examination, the underlying structural dynamic characteristics of interest are verified. Specifically, the attenuation zones in the experimental data for the compliant mechanism structure are present. However, the first attenuation zone has moved approximately 500 Hz higher and extends from 3000 to 5500 Hz. The large peak in the computed response at 7080 Hz has shifted to 8350 Hz in the experimental data. The reduction in the computed response at 8200 Hz, which leads into the beginning of the second attenuation zone, is present in the experimental data from approximately 9600 Hz to 10 kHz.

Within each attenuation zone a significant reduction in the measured response of the compliant mechanism structure is evident relative to that of the reference square core structure. This direct comparison of experimental data is made in Fig. 16. Analysis of the data for the compliant mechanism structure reveals an average rms transverse velocity level of 72.1 dB over the frequency range spanning 3000–5500 Hz. For the square core structure the average rms transverse velocity is 88.9 dB over the same frequency range. This represents a 16.8 dB reduction in the response of the compliant mechanism structure within the first attenuation zone, where maximum attenuation upwards of 45 dB is seen at 3460 Hz. From 9600 Hz to 10 kHz the experimental data average rms transverse velocity is 92.7 dB for the square core structure versus 72.2 dB

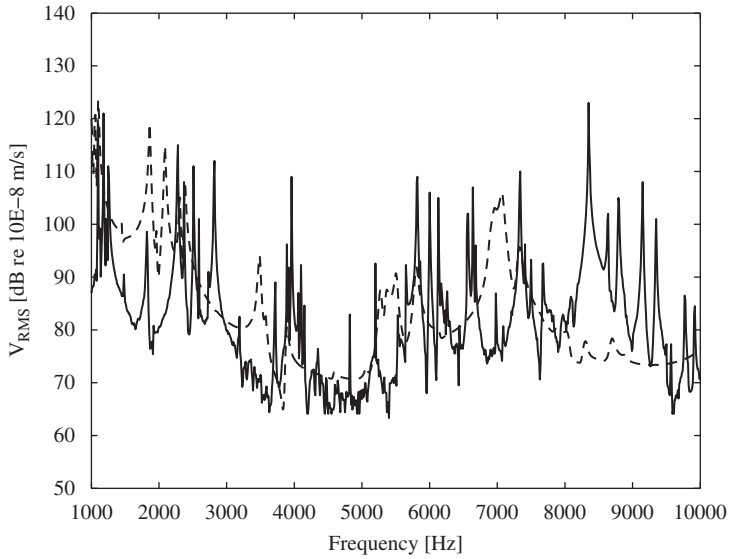


Fig. 15. Spectral finite element versus experimental root-mean-square transverse velocity (computed using the response from two top layer nodes) for compliant mechanism structure. (– –) Spectral data, (——) experimental data.

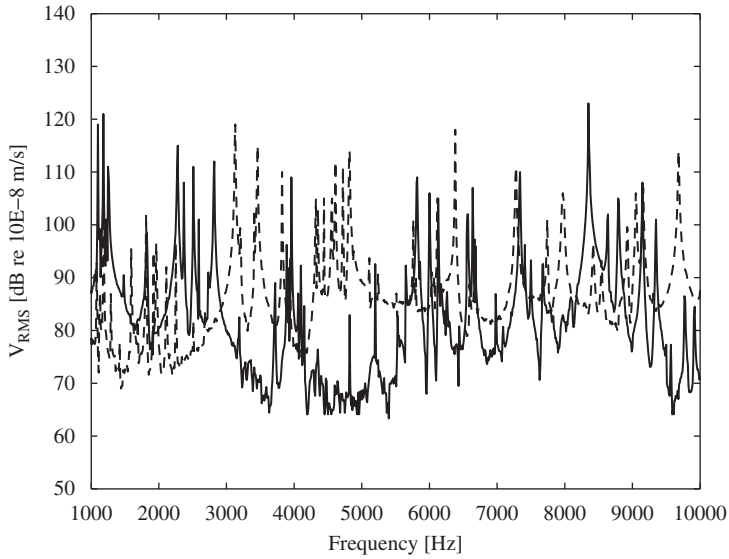


Fig. 16. Experimental root-mean-square transverse velocity comparison (computed using the response from two top layer nodes). (– –) Square core structure, (——) compliant mechanism structure.

for the compliant mechanism structure, which represents a reduction of 20.5 dB within the start of the second attenuation zone.

### 4.2. Two-dimensional continuum finite element analysis

As can be seen clearly in Figs. 12 and 13, the interfaces between the members that comprise each structure are not the ideal point connections assumed using one-dimensional spectral elements. Instead, these connections have a continuum nature and a non-zero fillet, which are consequences of the chosen manufacturing process. These radii act to stiffen response. Accordingly, to better capture this continuum

characteristic, a conventional two-dimensional finite element analysis using continuum elements was performed.

In the conventional finite element model the nodal load equivalent to the localized incident pressure wave on a bottom layer element of the structure is found in a manner similar to that for the spectral method:

$$\mathbf{f}^e(\mathbf{w}_b, \omega) = \int_0^{L^e} \mathbf{w}_b(x, \omega) p_{\text{in}} \, \mathrm{d}x, \tag{6}$$

where, in this instance, $\mathbf{w}_b$ is the conventional weighting function for a continuum shell element.

A *Nastran* Direct Frequency Response analysis using the SOL 108 solution sequence was performed over a 1–10 kHz frequency range in 10 Hz frequency steps. The compliant mechanism structure was modeled using 17,152 CQUAD4 elements. A similar analysis was performed for the reference square core structure using 11,556 elements. The localized bottom layer nodal loading applied to each structure was once more calculated from a excitation sound pressure level of 145.4 dB re 20E − 6 Pa.

### 4.3. Comparison of experiment and continuum finite element analyses

Figs. 17 and 18 give the computational and experimental results for the square core structure and compliant mechanism structure, respectively. Neglecting frequency dependent effects, a constant structural damping parameter of 0.003 was assumed in order to provide the best general fit between the analysis and the measured data in terms of resonant peak amplitude. A visual inspection of these figures shows that the incidence of resonances, anti-resonances, and minima are generally in agreement over the breadth of the test frequency range, thus substantiating the refined computational approach.

To illustrate the expected non-resonant performance of the compliant mechanism structure the computed deformed shape of the sandwich beam is shown at a frequency within the first attenuation zone in Fig. 19 (4600 Hz). This figure depicts the manner in which large motion of the structure's bottom layer is converted into reduced motion of the structure's top layer via the inherent amplification properties of the periodic core of the structure. In contrast, the primary limiting factor for the first attenuation zone is the global mode at 3963 Hz (obtained using a *Nastran* SOL 103 Normal Modes analysis) shown in Fig. 20, which is predicted by the frequency response data and results in larger normal velocity response amplitude.

Differences between the computed and measured rms transverse velocity response for each structure are shown in Figs. 21 and 22. Over the 1–10 kHz frequency range the measured response of the reference square

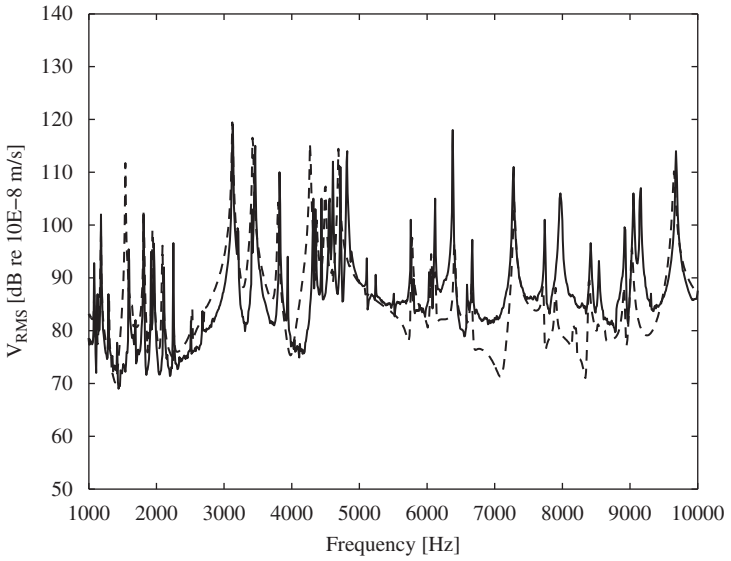


Fig. 17. *Nastran* versus experimental root-mean-square transverse velocity (computed using the response from two top layer nodes) for square core structure. (– –) *Nastran* data, (——) experimental data.

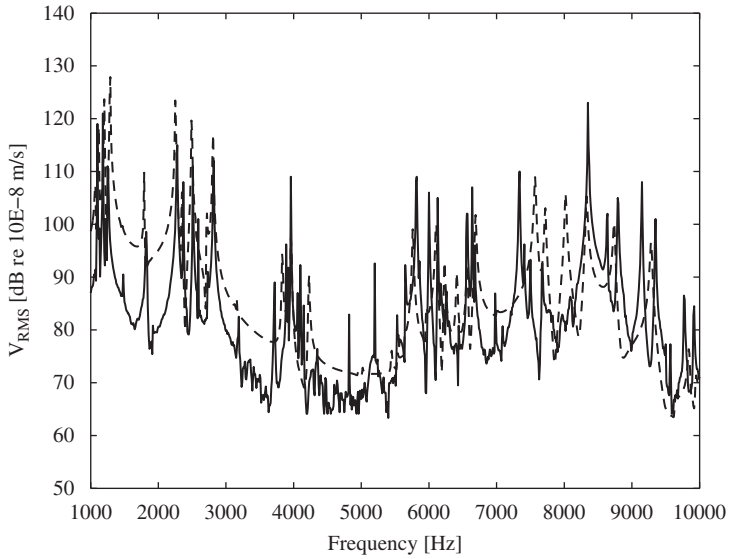


Fig. 18. *Nastran* versus experimental root-mean-square transverse velocity (computed using the response from two top layer nodes) for compliant mechanism structure. (– –) *Nastran* data, (——) experimental data.

Fig. 19. Non-resonant deformed shape of compliant mechanism structure (4600 Hz).

Fig. 20. Resonant mode shape of compliant mechanism structure (3963 Hz).

core structure differs from the *Nastran* computed response on average by 5.92 dB as shown in Fig. 21. For the prototype compliant mechanism structure the average difference between the measured data and the computed response is 8.43 dB, per Fig. 22.

Likely sources of error are highlighted in these figures. There are slight (i.e. generally ranging from 10 to 70 Hz) shifts of resonant frequencies relative to the computational analysis. In both analysis and experiment, a 10 Hz frequency step was employed, which allowed for acceptable resolution given the very large breadth of the overall frequency range. Nonetheless, slight shifts in resonant peaks are likely attributable to the lack of fine scale fidelity.

The presence of anti-symmetric or double modes also is clear based on the normal modes analysis performed for each structure. It is well known that perfectly symmetric, periodic structures become quasi-periodic once minor manufacturing tolerances and slight test setup misalignments are introduced [24,25]. Disorder effects redistribute energy, exciting anti-symmetric or double modes that do not exist in a computational analysis where the geometry, boundary conditions, and loading are assumed to be perfectly symmetric. Furthermore, in the case of the compliant mechanism structure, the acoustic excitation is applied at a location of relatively high flexibility. This results in possible local effects that, coupled with quasi-periodicity, excite anti-symmetric modes.

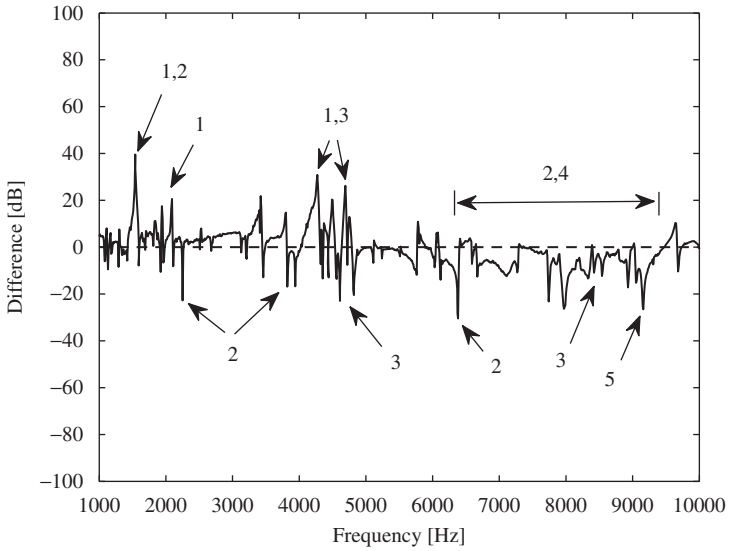


Fig. 21. Difference between *Nastran* and experimental root-mean-square transverse velocity results for square core structure. Average difference = 5.92 dB. Regions of interest are marked and the corresponding notes are: (1) slight shifting of resonant frequencies, (2) larger/sharper peaks, (3) due to anti-symmetric modes, (4) analysis generally under-predicts, (5) possible torsional mode.

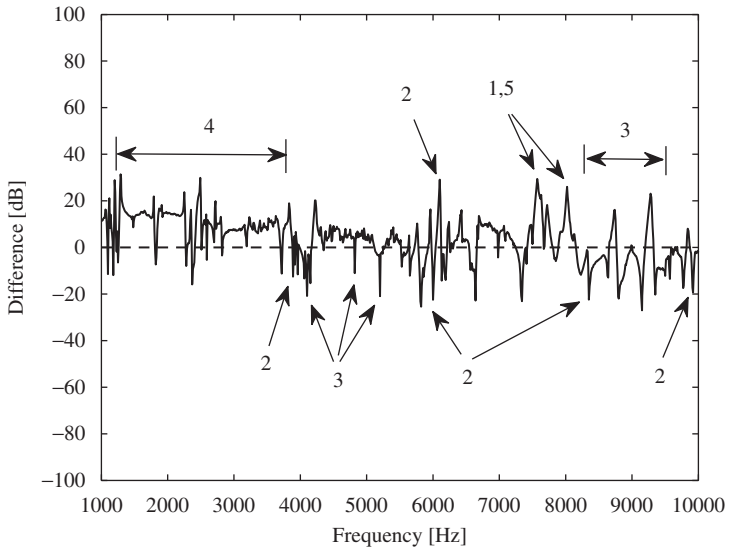


Fig. 22. Difference between *Nastran* and experimental root-mean-square transverse velocity results for compliant mechanism structure. Average difference = 8.43 dB. Regions of interest are marked and the corresponding notes are: (1) slight shifting of resonant frequencies, (2) larger/sharper peaks, (3) due to anti-symmetric modes, (4) analysis generally over-predicts, (5) less prominent resonant frequencies.

Fig. 23. Symmetric resonant mode shape of compliant mechanism structure (8739 Hz).

The close proximity of symmetric and anti-symmetric normal mode frequencies is seen in Fig. 23 (i.e. 8739 Hz) and Fig. 24 (i.e. 8797 Hz), respectively. Each figure presents modal results from the normal modes analysis. In Fig. 25 a zoomed view of the computational versus experimental rms normal velocity

Fig. 24. Anti-symmetric resonant mode shape of compliant mechanism structure (8797 Hz).

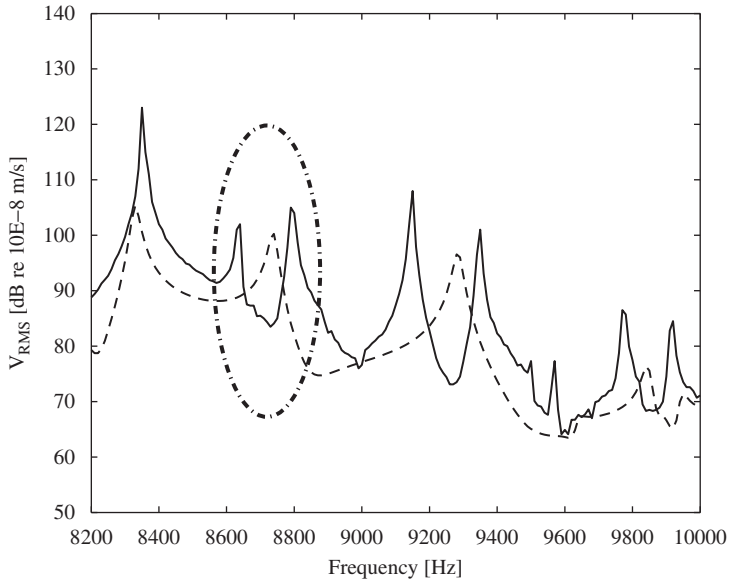


Fig. 25. *Nastran* versus experimental root-mean-square transverse velocity (computed using the response from two top layer nodes) for compliant mechanism structure. (– –) *Nastran* data, (——) experimental data, (– · –) highlighted region.

response of the compliant mechanism structure is given from 8200 to 10,000 Hz. The direct frequency response analysis also predicts the symmetric resonant peak at 8739 Hz highlighted in this figure, but not the anti-symmetric peak at 8797 Hz. However, the experimental data in this figure shows the separation of the symmetric mode into two modes occurring at 8650 and 8790 Hz. Thus, the experimental data confirms the presence of two modes very close to each other in this frequency range and splitting the computed peak into two. This final source of error is visible at other locations (e.g. at 9290 Hz in Fig. 25) throughout the 1–10 kHz frequency range for each structure and accounts for several outlying values.

## 5. Conclusions

A detailed study of the mid-frequency dynamic behavior of a prototype sandwich beam structure containing periodic integral compliant mechanisms was described in this paper. The rms normal velocity response of the compliant mechanism structure was computed at multiple scales using the spectral finite element method and was contrasted with that of a reference square core structure. The fabrication and experimental testing of both structures was then discussed. Qualitative and quantitative comparisons were made between the spectral computational and experimental data for each structure. Furthermore, the broadband attenuation zones of the compliant mechanism structure were verified and limitations of the spectral approach were delineated. Lastly, these limitations led to the logical implementation of a refined conventional finite element computational analysis for more complete validation of the experimentally measured data and further identification of sources of measurement error.

Thus, to summarize, the cumulative results from the numerous aforementioned studies suggest a two stage design process. In the first stage, the one-dimensional spectral method is employed to design the basic compliant mechanism unit cell and structure. A subsequent, two-dimensional analysis should then be

completed, utilizing the manufactured mechanism design to identify the most significant variations from the idealized one-dimensional analytical prototype.

The integration of compliant mechanisms into structural–acoustic sandwich panels of lightweight automotive, aerospace, and naval vehicles has much potential. The truss-like nature of these structures suggests multi-functionality including the possibility of combining vibro-acoustic and load bearing capabilities. Current computational work involving extensions to three-dimensional sandwich structures is ongoing. Interesting applications and broader manufacturing approaches at smaller scales may also arise when the scope of this work is extended to include analysis in the nonlinear regime along with the use of alternative materials such as polymers, composites, and biological tissues.

## References


[1] J. Oberg, Orbital shouting—noise becomes an issue on the International Space Station, *Scientific American* 287 (1) (2002) 26–27.

[2] W.V. Bhat, Flight test measurement of exterior turbulent boundary layer pressure fluctuations on Boeing model 737 airplane, *Journal of Sound and Vibration* 14 (4) (1971) 439–457.

[3] W.V. Bhat, J.F. Wilby, Interior noise radiated by an airplane fuselage subjected to turbulent boundary layer excitation and evaluation of noise reduction treatments, *Journal of Sound and Vibration* 18 (4) (1971) 449–464.

[4] M. El-Raheb, P. Wagner, Transmission of sound across a trusslike periodic panel; 2-D analysis, *The Journal of the Acoustical Society of America* 102 (4) (1997) 2176–2183.

[5] M. Ruzzene, F. Scarpa, F. Soranna, Wave beaming effects in two-dimensional cellular structures, *Smart Materials and Structures* 12 (3) (2003) 363–372.

[6] M. Ruzzene, Vibration and sound radiation of sandwich beams with honeycomb truss core, *Journal of Sound and Vibration* 277 (4–5) (2004) 741–763.

[7] M. El-Raheb, Frequency response of a two-dimensional trusslike periodic panel, *The Journal of the Acoustical Society of America* 101 (6) (1997) 3457–3465.

[8] L. Brillouin, *Wave Propagation in Periodic Structures: Electric Filters and Crystal Lattices*, first ed., McGraw-Hill, New York, 1946.

[9] D.J. Mead, S. Parthan, Free wave propagation in two-dimensional periodic plates, *Journal of Sound and Vibration* 64 (3) (1979) 325–348.

[10] R.S. Langley, The response of two-dimensional periodic structures to point harmonic forcing, *Journal of Sound and Vibration* 197 (4) (1996) 447–469.

[11] J. Fish, W. Chen, G. Nagai, Non-local dispersive model for wave propagation in heterogeneous media: multi-dimensional case, *International Journal for Numerical Methods in Engineering* 54 (3) (2002) 347–363.

[12] P.G. Martinsson, A.B. Movchan, Vibrations of lattice structures and phononic band gaps, *Quarterly Journal of Mechanics and Applied Mathematics* 56 (1) (2003) 45–64.

[13] M.I. Hussein, G.M. Hulbert, R.A. Scott, Dispersive elastodynamics of 1D banded materials and structures: analysis, *Journal of Sound and Vibration* 289 (4–5) (2006) 779–806.

[14] S. Halkjaer, O. Sigmund, J.S. Jensen, Maximizing band gaps in plate structures, *Structural and Multidisciplinary Optimization* 32 (4) (2006) 263–275.

[15] KMODDL page: model S39 rhombus straight-line linkage, from ⟨http://kmoddl.library.cornell.edu/model.php?m=160⟩, 3 August 2006.

[16] L.L. Howell, *Compliant Mechanisms*, Wiley, New York, 2001.

[17] S. Kota, J.Y. Joo, Z. Li, S.M. Rodgers, J. Sniegowski, Design of compliant mechanisms: applications to MEMS, *Analog Integrated Circuits And Signal Processing* 29 (1–2) (2001) 7–15.

[18] U.D. Larsen, O. Sigmund, S. Bouwstra, Design and fabrication of compliant micromechanisms and structures with negative Poisson's ratio, *Journal of Microelectromechanical Systems* 6 (2) (1997) 99–106.

[19] E.M. Dede, G.M. Hulbert, Analysis, design, and optimization of structures with integral compliant mechanisms for mid-frequency response, *International Journal for Numerical Methods in Engineering* 73 (4) (2008) 470–492.

[20] J.F. Doyle, *Wave Propagation in Structures: an FFT-based Spectral Analysis Methodology*, Springer, New York, 1989.

[21] Knovel page: military handbook—MIL-HDBK-5H: metallic materials and elements for aerospace vehicle structures, from ⟨http://www.knovel.com/knovel2/Toc.jsp?BookID=754⟩, 3 August 2006.

[22] Y.M. Amraoui, N.A.J. Lieven, Noncontacting excitation and measurement of light structures, *Journal of Vibration and Acoustics—Transactions of the ASME* 125 (1) (2003) 114–119.

[23] H. Van der Auweraer, P. Vanherck, P. Sas, R. Snoeys, Accurate modal analysis measurements with programmed sine wave excitation, *Mechanical Systems and Signal Processing* 1 (3) (1987) 301–313.

[24] D.J. Ewins, *Modal Testing: Theory, Practice, and Application*, second ed., Research Studies Press, Philadelphia, 2000.

[25] C. Pierre, M.P. Castanier, W.J. Chen, Wave localization in multi-coupled periodic structures: application to truss beams, *Applied Mechanics Reviews* 49 (2) (1996) 65–86.